Effects of roughness on rarefied gas flow in a microfluidic channel with porous walls

Amirreza Soheili[1, §, *], Arsha Niksa[2, ‡, *], Vahid Bazargan[1, †]

[1]*University of Tehran, Department of Mechanical Engineering, Tehran, Iran*

[2]*Mofid Educational Complex, Department of Physics and Mathematics, Tehran, Iran*

Corresponding Author: Amirreza Soheili

Email Address: asoheili@ut.ac.ir

• Abstract

This study attempts to investigate the effect of roughness on rarefied gas flow inside microchannels with rough walls. The model presented in this paper makes use of a microchannel with cuboid geometry. In this simplified microchannel, the rough walls have been modelled as porous media, which are assumed to exhibit a similar behavior to rough surfaces. Using this simplification, both Navier-Stokes and Darcy-Brinkman equations were used to derive analytical solutions for velocity profile, pressure distribution, and mass flowrate inside the microchannel. Subsequently, these analytical solutions were plotted and numerically visualized to study the effects of the inverse Knudsen number, porous media thickness and permeability on the gas flow from a theoretical point of view. Furthermore, a separate means of numerically simulating the porous interface inside the microchannel was implemented via COMSOL Multiphysics to to cross-check the analytical solution. The results of the COMSOL simulation were, then, compared with the numerical visualizations of our analytical results to provide ground for comparison between these two. This comparative study showed agreement between these two methods in velocity profile of the core region of the microchannel and the pressure distribution, while also demonstrating a disparity and difference between the predicted velocity profiles inside the porous regions. Ultimately, the reason behind this difference was investigated and hypothesized about.

Keywords: Roughness, rarefied gas flow, porous media, velocity profiles, mass flow rate, pressure distribution

• Article Highlights

- The velocity profiles were investigated inside both the core region of the microchannel and the porous media. Accordingly, it was found that the velocity inside the core region decreases as the fluid approaches the outlet of the microchannel. It is worthwhile to mention that this decrease was accompanied by a convex trend. As for the velocity inside the porous media, it was found out that similar to the velocity trend inside the core region, the velocity with respect to distance from the inlet decreases as well. It was also learnt that the velocity inside the porous media is orders of magnitude lower than the flow velocity in the core region.

- The pressure distribution in the microchannel was found to be decreasing as the fluid approaches the outlet of the microchannel. Similar to the velocity profiles, this behavior was theoretically predicted to be following a convex trend.

- The effects of the inverse Knudsen number, porous media thickness and permeability were also considered. Correspondingly, it was concluded that the inverse Knudsen number exhibits a proportional effect on the velocity of the fluid inside the porous media. Moreover, it appeared that as the thickness of porous media

§ asoheili@ut.ac.ir   (0000-0003-2565-5575)

‡ ar.niksa@outlook.com (0000-0001-7607-0492)

† vbazargan@ut.ac.ir

* Both authors contributed equally to this manuscript.

increased, the difference between the flow velocity in the core region and porous media increased, too. The permeability of the porous media also exhibited a similar behavior, where the difference between the fluid velocity inside the porous media and core region increased as permeability rose. Furthermore, it was surprisingly found that the pressure distribution varies negligibly with respect to variations in permeability and porous media thickness. However, an increase in the inverse Knudsen number was observed to lead to an increase in the pressure difference between inlet and outlet of a microchannel.

• Declarations

- **Funding:** No funding was received for this study.
- **Competing Interests:** The authors declare that they have no competing interests.
- **Availability of Data and Materials:** (Not Applicable)
- **Code and Software Availability:** The MATLAB code can be downloaded using this link. Please note that the code can be run using MATLAB r2019b. The authors do not guarantee backwards compatibility.
  The COMSOL Multiphysics simulation file can be downloaded using this link. Note that this simulation was run on COMSOL Multiphysics 5.5. Similar to the MATLAB code, the authors do not guarantee backwards compatibility.

1. INTRODUCTION

Understanding the effect of surface roughness on fluid flow in microchannels has a significant importance due to high application of microfluidic devices in recent years. The wide variety of microchannels applications give high significance to these miniaturized technologies, obliging us to understand different gaseous behaviors that might be exhibited in microchannels, one of which is the effect of roughness on the behavior of fluid flow inside microchannels. In fact, there have been extensive investigations into the effect of roughness on our subjects of study [1-3].

One of these unusual behaviors is demonstrated when the characteristic length of a microchannel becomes comparable to the molecular free path inside the channel, inducing the effects that become observable due to roughness and gas rarefaction [4]. Accordingly, it would be necessary to understand this unique phenomenon to further improve technologies that rely on microchannels, such as heat exchangers, chemical reactors, cryogenic systems, and so forth [5-9].

Various methods have been used to investigate roughness microchannel walls. In some cases, empirical models were developed to theoretically explain the phenomenon. Gamrat et al. [10] studied the influence of microchannel roughness on laminar flow by modeling roughness in the range of 100-300 micrometers in terms of the height of the rough areas. Tang et al. [11] developed an experimental apparatus for investigating how surface roughness and rarefaction influence nitrogen and helium flow in a fused silica microtube. Using the Electrical Discharge Method (EDM), Jones et al. [12] were able to reproduce controlled roughness, enabling them to study the effect of roughness

on flow boiling in microchannels. Wu et al. [13] investigated the effect of surface roughness on convective heat transfer in silicon microchannels.

In other works, utilization of numerical simulations is one of the most favorable methods which has been commonly implemented. Rawool et al. [14] devised a numerical simulation by modeling roughness as two obstruction shapes (triangle and rectangle) on channel walls and investigated its impact on the friction factor of the channel. Cao et al. [15] used a Molecular Dynamics (MD) simulation to investigate the effect of roughness on slip flow of argon in submicron platinum microchannels. Similarly, Peng et al. [16] also used an MD simulation which modeled roughness as spherical objects which argon considered to be working fluid under boiling conditions. Zarringhalam et al. [17] investigated the effect of surface roughness elements with cone geometry for argon flow in microfluidic devices using Molecular Dynamics. Croce et al. [18] modeled roughness as 3D conical peaks distributed on a plane microchannel, which was tested at various values of the Reynolds number. Chen et al. [19] conducted a 3D model of laminar flow by modeling surface roughness as fractal shapes. In the study conducted by Gamrat et al. [20], a 3D numerical simulation was used to investigate the effect of roughness on heat transfer in thermally fully-developed laminar flow inside microchannels. In their model, roughness was modeled as a pattern of parallelepipedic elements being periodically distributed on the plane walls of microchannels. Ji et al. [21] devised a 2D simulation for compressible gas flow in slip regime, modeling wall roughness through rectangular microelements. Khadem et al. [22] modeled surface roughness as distributed rectangular microelements and randomly-generated micropeaks distributed on the wall surface. Sun et al. [23] studied the effect of roughness on nitrogen flow using the Direct Simulation Monte Carlo (DSMC) method in which rectangular elements were used to mimic roughness. Wang et al. [24] investigated the effect of roughness on electro-osmotic flow behaviors in microchannels using the Lattice-Boltzmann method, in which roughness was modeled as a series of rectangular object which varied in height. Yang et al. [25] modeled sinusoidal roughness in microchannels and numerically simulated its effect on electro-osmotic fluid flow.

As discussed above, both empirical methods and numerical simulations were utilized to model surface roughness and investigate its effect on fluid flow in microchannels. In some cases, the roughness was modeled through the properties of a porous medium and as a result, the governing equations and relevant simulations were rearranged considering the characteristics of porous sections. W. Li et al. [26] theoretically modelled a circularly symmetric microchannel where the effect of roughness was mimicked by a porous film attached to the walls of the microchannel.

As for the flow inside the porous media, the Brinkman formulation of Darcy's law was employed, while the core region was mainly explicated by a slip-flow model. Accordingly, equations of velocity, flow rate, and pressure distribution were deduced and analytically solved.

A. E. Meyerovich and S. Stepaniants [27-28], however, tried to tackle this problem by a rather different approach. Instead of modelling the roughness by a porous film, the boundaries were given a statistical treatment, where the roughness was randomly generated. Yet, their theoretical model is valid for mostly high Knudsen numbers [29] and does not account for low Knudsen numbers.

This problem was tackled by G. Karniadakis et al. [29] who developed a model which could be used in low Knudsen numbers ($Kn = 0.17$). Subsequently, their model was numerically simulated which had the analytic power of predicting the pressure drop due to roughness.

In this paper, an approach similar to W. Li et al. [26] will be implemented, where the roughness is modeled as porous media. Yet, there are two key differences that make this study prominent. First, the corresponding equations will be developed for a cuboid geometry instead of a cylindrical geometry and the equations will be set Cartesian coordinates, instead. Second, a 2D simulation in the Free and Porous Media Flow Module of COMSOL Multiphysics has been employed, providing us with further insight into how velocity and pressure vary along the microchannel.

This paper is formatted in the following way: In Sec.2.a, the geometrical model of the microchannel is described. In addition to this, Sec.2.a includes an account of how both the Navier-Stokes and Darcy-Brinkman equations can be simplfiied based on a few assumptions. In Sec.2.b, these equations are analytically solved in order to provide us with the fluid velocity inside both the porous and core, non-porous regions. Moreover, the mass flow rate is also derived at the end of this subsection. In Sec.2.c, pressure along the microchannel is analytically derived. In Sec.3.a, numerical visualizations of pressure and velocity as functions of the inverse Knudsen number, porous media thickness and permeability are provided. In Sec.3.b, another simulation is presented, which has been designed using the the Free and Porous Media Flow Module of COMSOL Multiphysics to provide us with pressure and velocity in the microchannel. Subsequently, in Sec.3.c, one of the cases presented Sec.3.a-b is comparatively studied, where similarities and differences between the analytic and the COMSOL model are investigated. In Sec.4, a summary of our results is provided, in addition to hinting at possible future directions of this study.

2. THEORETICAL MODEL

a. Geometrical Model and Governing Equations

As previously stated, the general geometry of the microchannel is assumed to be cuboid, the length of which is L, while both the height and depth are equal to $2h$. The porous media, by which internal roughness is modelled, is assumed to be attached to the walls of the cube with a thickness of δ. The geometry of the microchannel is illustrated in Fig.1.
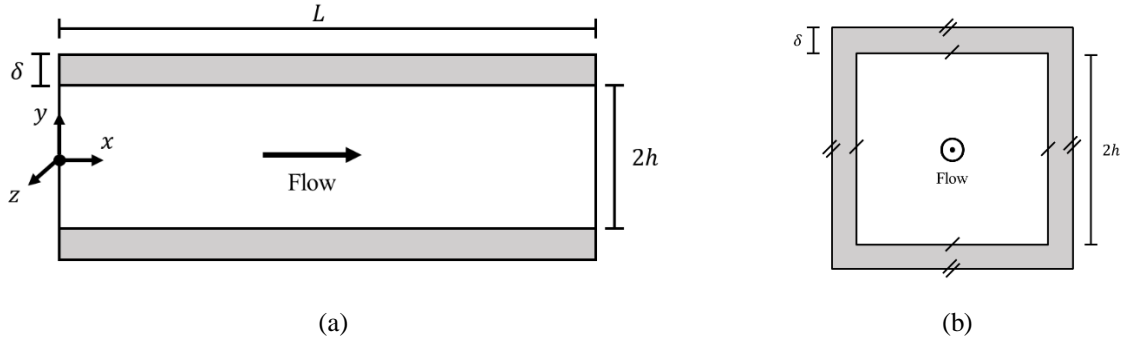

(a) (b)

Figure 1: (a) represents the sideways view of the microchannel, while (b) shows its cross section.

As demonstrated in Fig.1, the origin of the coordinate system, which is Cartesian, is set at the center of the cross section and coincides with the surface of the inlet.

Now that the geometric properties of the system are defined, we will move onto the introduction and simplification of the governing equations. In order to do this, we will start from the general form of the x-momentum Navier-Stokes equation, which is [30]

$$\rho\left(\frac{\partial u}{\partial t} + u\frac{\partial u}{\partial x} + v\frac{\partial v}{\partial y} + w\frac{\partial w}{\partial y}\right) = -\frac{dp}{dx} - \frac{\partial \tau_{xx}}{\partial x} - \frac{\partial \tau_{yx}}{\partial y} - \frac{\partial \tau_{zx}}{\partial z} + F_x \tag{1}$$

where u, v, and w represent flow velocity along the x, y, and z axis, ρ shows fluid density, p is pressure and τ_{xx}, τ_{yx}, and τ_{zx} are shear stress constitutive equations, which are defined as

$$\tau_{xx} = -\mu\left(2\frac{\partial u}{\partial x} - \frac{2}{3}\nabla.\vec{U}\right) \tag{2}$$

$$\tau_{yx} = -\mu\left(\frac{\partial u}{\partial y} + \frac{\partial v}{\partial x}\right) \tag{3}$$

$$\tau_{zx} = -\mu\left(\frac{\partial u}{\partial z} + \frac{\partial w}{\partial x}\right) \tag{4}$$

where μ shows the viscosity of the fluid.

By assuming that the flow is stationery, the first and second term of the left-hand side of Eq.1 will be crossed out. Besides that, both the third and fourth will be also crossed out as v and w are presumed to be negligibly small.

Regarding the right-hand side of Eq.1, both the second, third, and fourth terms are assumed to be equal to 0, owing to the stationery condition of the flow and the negligibility of v and w. Moreover, F_x will also be crossed out as no external forces are present.

As a result, Eq.1 could be rewritten as

$$\frac{dp}{dx} = \mu \frac{\partial^2 u}{\partial y^2} \tag{5}$$

Note that Eq.4 accounts for the flow in the core region and is not readily expanded to the porous film media. To resolve this problem, we will rewrite Eq.4 using the Brinkman formulation of Darcy's law [31-33], yielding

$$\frac{dp}{dx} = \mu \frac{\partial^2 \tilde{u}}{\partial y^2} - \frac{\tilde{\mu}}{k} \tilde{u} \tag{6}$$

where k is the permeability of the porous film, $\tilde{u}$ shows velocity along the x-axis, and $\tilde{\mu}$ is the viscosity of the fluid in the porous film, which we will assume to be equal to μ for simplicity.

b. Derivation of Fluid Velocity and Mass Flow Rate

Now that we have obtained Eqs.5-6 for both the core region and the porous media, we could solve for the velocity profiles of both regions. This provides us with

$$u = \frac{y^2}{2\mu} \frac{dp}{dx} + C_1 y + C_2 \tag{7}$$

$$\tilde{u} = -\frac{k}{\tilde{\mu}} \frac{dp}{dx} + C_3 y + C_4 \tag{8}$$

where C_1, C_2, C_3, and C_4 are constants. Note that C_1 is equal to zero for finite flow along the x-axis at $y = 0$ and $z = 0$.

In order to derive the constant values in Eqs.7-8, we have to define our boundary conditions. Subsequently, these boundary conditions can be used to solve for the constant values in Eqs.7-8.

The boundary conditions, which are given by using the high-order slip flow model in addition to the stress continuity condition [34], are

$$\mu \frac{\partial u}{\partial y}\Big|_{y=|h|} = \tilde{\mu} \frac{\partial \tilde{u}}{\partial y}\Big|_{y=|h|} \tag{9}$$

$$u|_{y=|h|} = \tilde{u}|_{y=|h|} - a\lambda D^d \frac{\partial u}{\partial y}\Big|_{y=|h|} - \frac{b}{2} D^c h^2 \frac{\partial^2 u}{\partial y^2}\Big|_{y=|h|} \tag{10}$$

$$\tilde{u}|_{y=|h+\delta|} \approx 0 \tag{11}$$

where λ is the mean free path, D is the inverse Knudsen number ($D = \frac{2\sqrt{2}\pi h}{\lambda}$), and $a = 0.49, b = 1.28, c = -1.0669$, and $d = -0.003$ are coefficients.

With the definition of our boundary conditions, we are able to insert Eqs.9-11 in Eqs.7-8, allowing us to obtain the constant values. The results would be

$$C_2 = \frac{dp}{dx} \frac{h^2}{2\mu}\left(1 - \frac{2k}{h^2} - 2a\lambda \frac{D^d}{h} - bD^c\right) \tag{12}$$

$$C_3 = \frac{dp}{dx} \frac{h}{\mu} \tag{13}$$

$$C_4 = \frac{dp}{dx} \frac{1}{\mu}(k - (h+\delta)h) \tag{14}$$

Now that the velocity profiles have been defined, we can deduce the mass flow rate by integrating the complete forms of Eqs.7-8 by their corresponding cross section and then multiplying them by ρ. This would provide us with

$$\dot{m} = 2\frac{\rho h^4}{\mu} \frac{dp}{dx}\left(\frac{4}{3} - \frac{2k}{h^2} - a\lambda \frac{D^d}{h} - bD^c\right) \tag{15}$$

$$\tilde{\dot{m}} = -4\frac{h\delta^2}{\mu} \frac{dp}{dx}(h+\delta) \tag{16}$$

c. Derivation of Pressure along the Microchannel

To derive the pressure distribution, we have to start from the equations of continuity for both core and porous regions, which are

$$\frac{\partial \rho}{\partial t} + \frac{\partial(\rho u)}{\partial x} + \frac{\partial(\rho v)}{\partial y} + \frac{\partial(\rho w)}{\partial z} = 0 \tag{17}$$

$$\frac{\partial \rho}{\partial t} + \frac{\partial(\rho \tilde{u})}{\partial x} + \frac{\partial(\rho \tilde{v})}{\partial y} + \frac{\partial(\rho \tilde{w})}{\partial z} = 0 \tag{18}$$

Based on the assumption that fluid velocity along the y and z axes is negligible, both the third and fourth terms of Eqs.17-18 will be crossed out. Moreover, the stationery condition of the system would cause $\frac{\partial \rho}{\partial t}$ to be equal to zero. Thus, Eqs.17-18 can be rewritten as

$$\rho \frac{\partial u}{\partial x} + u \frac{\partial \rho}{\partial x} = 0 \tag{19}$$

$$\rho \frac{\partial \tilde{u}}{\partial x} + \tilde{u} \frac{\partial \rho}{\partial x} = 0 \tag{20}$$

After integrating Eqs.19-20 over their corresponding cross section, adding them together, and integrating the result twice with respect to *x*, we obtain

$$\rho \frac{p}{\mu}(4h^2 + \delta^2)\left(\frac{y^2 + h^2 - bD^c h^2}{2} - k - a\lambda D^d h\right) = C_5 x + C_6 \tag{21}$$

where C_5 and C_6 are integration constants.

To deduce these constant values, the microchannel inlet and outlet boundary conditions will be used. These boundary conditions, which are deducible from the equation for an ideal gas [26], are

$$D|_{x=0} = D_i \tag{22}$$
$$D|_{x=L} = D_o \tag{23}$$

where $D = D_o P, P = {p}/{p_0}$, $D_i = D_o \Pi$, $D_o = \frac{2\sqrt{2}\pi h}{\lambda}$, and $\Pi = {p_i}/{p_o}$. Note that i and o represent inlet and outlet, respectively.

After solving Eq.21 for the constants using the boundary conditions, namely Eqs.22-23, the integration constants would be defined as

$$C_5 = \rho \frac{p}{\mu L}(4h^2 + \delta^2)\left(\frac{b}{2}h^2 D_o^c\left(\Pi^c - (\frac{p}{p_o})^c\right) + a\lambda h D_o^d\left(\Pi^d - (\frac{p}{p_o})^d\right)\right) \tag{24}$$

$$C_6 = \rho \frac{p}{\mu}(4h^2 + \delta^2)\left(\frac{y^2 + h^2 - b(D_o \Pi)^c h^2}{2} - k - a\lambda (D_o \Pi)^d h\right) \tag{25}$$

As a result of this derivation, the pressure distribution can be defined through Eq.21, providing us another key component of the system, which can be used to describe the fluid flow inside the microchannel.

3. Numerical Models

a. Numerical Visualization via MATLAB

In this subsection, Eqs.7-8,15-16, and 21 would be numerically plotted using the Matrix Laboratory (MATLAB) to allow for qualitative comparison between a variety of parameters, namely porous thickness, porous permeability and the inverse Knudsen number.

In Fig.2, the velocity at different inverse Knudsen numbers (a-d), porous media permeabilities (a-d), and porous media thicknesses (e) have been explored. Note that the majority of the numbers in the following graphs were implemented based on the values which Li et al. [26] have used for their graphs. However, a few changes were made to allow for a rather comprehensive visualization.
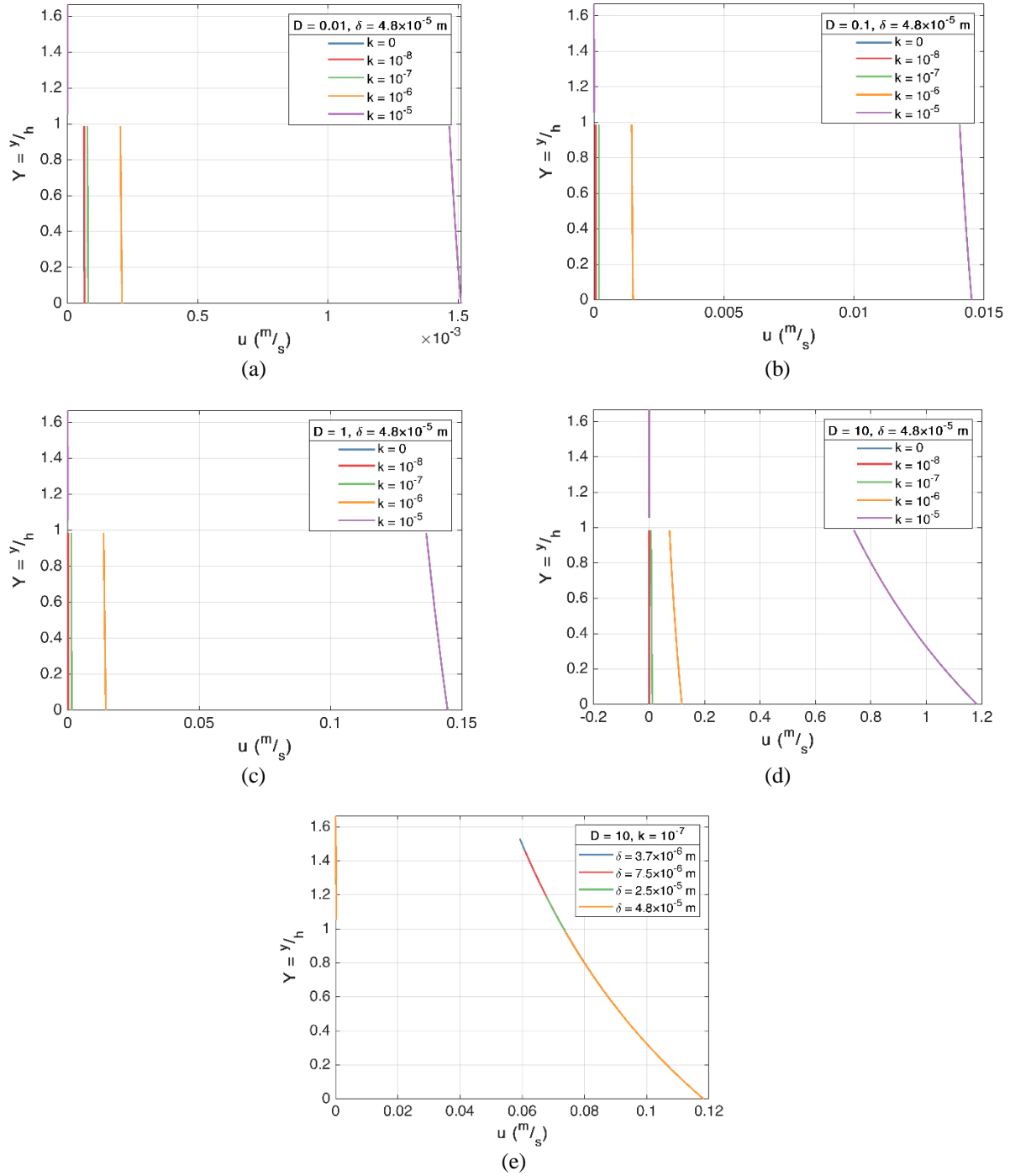
Figure 2: In (a-d), both the inverse Knudsen number and permeability have been changed, porous media thickness was changed in (e). Please note that the asymmetric values of the velocity profile at negative values of Y have been dismissed due to incompatibility with our assumptions.

Furthermore, the velocities at porous regions, namely $\tilde{u}$, have been shown with the same symbol as core velocity values, u. These two can be distinguished by their range, where $Y > 1$ belongs to $\tilde{u}$, even though $0 \leq Y \leq 1$ corresponds to u.

As seen in Fig.2, one of the most predominant characteristics of the velocity profile is the considerable velocity difference between the core and porous regions. Put differently, the velocity of the fluid inside the porous region seems to be near zero, while also showing a negligible degree of change with respect to Y, which is the ratio of y against h. Note that even though the velocity in the porous region (which is demonstrated as values of u at $Y > 1$), the velocity does vary along different values of Y. To better understand this, rescaled versions of velocity in the porous regions have been visualized in App.A.

Contrary to the relatively lower values in the porous regions, the velocity is visibly varying with respect to Y and increases as the value of Y approaches zero. Under the assumption that the velocity profile is symmetric, this result would indicate that the velocity of the gaseous fluid increases as at areas closer to the center of microchannel. Moreover, the trend in the core region seems to follow a behavior similar to a convex function, where the change in velocity decreases at areas close to the center of the microchannel.

Moving onto the variations of relevant parameters and their relation to the velocity profiles, we can infer from Figs.2.a-d, where the inverse Knudsen number varies and is the subject of study, that the order of magnitude of core velocity seems to increase as D increases. In the transition regime between continuum and slip flow, which is indicated by $D = 0.01$ in Fig.2.a, the order of magnitude of velocity inside the core region is at approximately 10^{-3} m/s. At the inverse Knudsen number located in the transition between slip and early transition regimes, which corresponds to $D = 0.1$ in Fig.2.b, the core velocity order of magnitude is at around 10^{-2} m/s. Finally, at values of D which are between early transition and transition flow ($D = 1$ in Fig.2.c) and also between transition and free molecular flow ($D = 10$ in Fig.2.d), the core velocity values are at approximately 10^{-1} m/s and 10^0 m/s, respectively.

Another noticeable thing with respect to different inverse Knudsen numbers is the apparent increase in the relative difference between core velocities at $0 \leq Y \leq 1$. Put differently, as the value of D increases in Figs.2.a-d, the difference between the core velocity at $Y = 0$ and the core velocity at $Y = 1$ seems to relatively increase.

This behavior is also visible at difference values of permeability, k, which are demonstrated in Figs.2.a-d separately. In other words, as the permeability increases, the difference between $u|_{Y=0}$ and $u|_{Y=1}$ increases. In addition to this, different values of k seem to yield different values of $u|_{Y=0}$. This is demonstrated by how higher values of permeability lead to higher velocities at $Y = 1$. This can be also interpreted as a bigger gap between the velocities between the

porous and core regions, which can be seen at $Y = 1$. Please note that the reason behind choosing lower values of permeability for Fig.2 can be explained by how our model has analytic power at very low permeabilities and on the contrary, overpredicts velocity at larger values of k.

In Fig.2.e, the main focus of the graph is variations in the thickness of the porous films attached to the walls of the microchannel. Contrary to the Figs.a-d where $\delta = 4.5 \times 10^{-5}\ m$, the majority of the lines in this figure bar the orange line, seem to lack the gap between velocity values between core and porous regions. Put differently, as the porous film thickness decreases, velocity at $Y = 1$ seems to become rather continuous. This can be interpreted as how the effect of porous film become subjectively negligible as its thickness decreases. The other remarkable point is that unlike Figs.2.a-d, the velocity in porous regions changes considerably in the porous regions, too. It is worthwhile to mention that the core velocity at $0 \leq Y \leq 1$ have all been masked by the orange line at $\delta = 4.5 \times 10^{-5}\ m$, hence the visibility of only one line.

Now that the velocity profile as functions of the inverse Knudsen number, porous media thickness and permeability has been investigated, we will move onto the pressure, p, along the microchannel at different inverse Knudsen numbers, which has been illustrated in Fig.3.
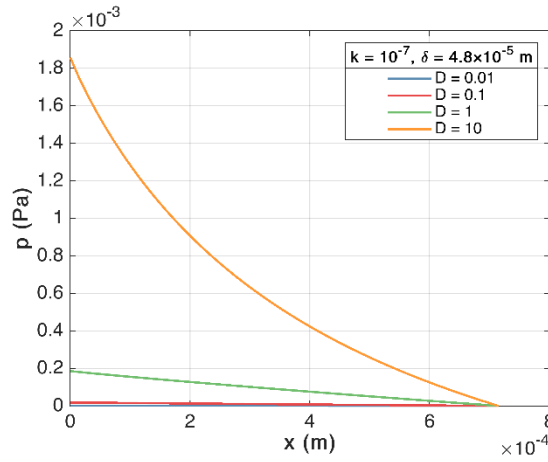
Figure 3: (a) represents the pressure along the microchannel at different inverse Knudsen numbers. The initial conditions were $p_{inlet} = 0.003\ Pa$ and $p_{outlet} = 0.002\ Pa$.

As demonstrated in Fig.3, as the inverse Knudsen number increases, the difference between outlet and inlet pressure seems to increase, which can be also be inferred from how the average slopes of lines tangent to the pressure lines occupy higher values at larger values of D. Moreover, what is interesting is that the difference between the initial inlet

pressure at $x = 0$ seems to get larger as the inverse Knudsen number increases, which can be interpreted as a larger

gap and thus, pressure drop at $x = 0$.

Note that pressure at different porous film thicknesses, δ, and different permeabilities, k, have not been included in

Fig.3 as they had none to negligible effect on the pressure along the microchannel. Pressure at different values of δ

and k, however, has been visualized in App.B for further demonstration of this matter.

b. Simulation via COMSOL Multiphysics

In this subsection, we will simulate a 2D interface of the microchannel in COMSOL Multiphysics and then, plot

filled contours of both velocity and pressure along the microchannel to allow for rather in-depth visualization. One of

the reasons behind employing this simulation is to cross-check the results presented in Sec.3.a. In order to access the

governing equations used in this module, please refer to Ref.a.

In this simulation, the Free and Porous Media Flow (FP) module of COMSOL Multiphysics was used to mimic a

2D representation of the microchannel similar to Fig.1.a. A visual illustration of the the geometry of the microchannel

and the relevant boundary conditions is demonstrated in Fig.4.

No-slip

	Porous Region	
Pressure-driven Inlet	Core Region	Pressure-driven Outlet
	Porous Region	

No-slip
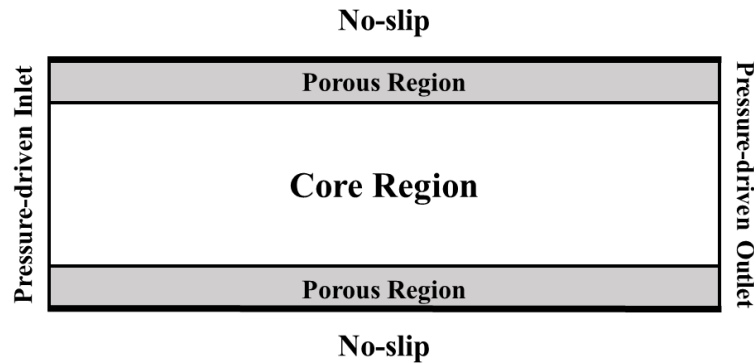
Figure 4: This figure demonstrates a geometrical representation of the microchannel in COMSOL Multyphysics along with relevant boundary conditions.

Using a stationery solver and applying it to the layout presented in Fig.4, the velocity profile in addition to pressure

along the microchannel was deducible. These two variables have been demonstrated in Fig.5 as filled contours.
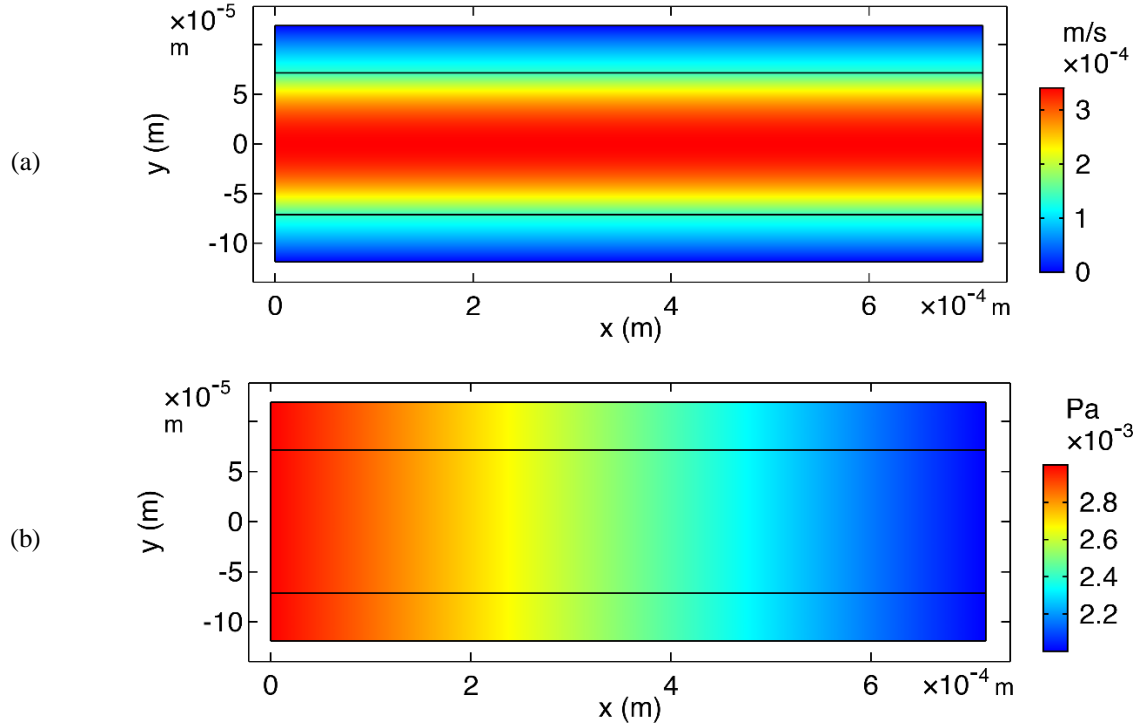
Figure 5: (a) shows the velocity contour in the microchannel, while (b) shows pressure along the microchannel. Note that the rectangular boxes at the bottom and top sections of the contour graphs represent porous regions.
Note that these graphs correspond to only one particular case where $k = 10^{-7}$, $\delta = 4.8 \times 10^{-5}\ m$, and $\phi = 0.38$, where ϕ shows porosity of the porous region.

As demonstrated in Fig.5.a, the velocity contour seems to hint at a fully-developed flow at $y = 0$. In addition to this, the velocity profile is symmetric with respect to the line corresponding to $y = 0$, which is expected on the account of our simplifying assumptions in Sec.2.a. It is worthwhile to mention that the minimum velocity in Fig.5.a is $u_{min} = 0$, while the maximum value of velocity is $u_{max} = 3.4 \times 10^{-4}\ ^m/_s$.

Besides to Fig.5.a, where the velocity contour was illustrated, pressure along the microchannel has also been visualized in Fig.2.b, where the pressure contour seems to follow a linearly decreasing trend from the inlet to the outlet. Furthermore, there seems to be now pressure drop at $x = 0$, which is contrary to the prediction provided by our analytical model visualizations in Sec.3.a. It is, again, necessary to mention that the minimum and maximum values of pressure in Fig.5.b are $p_{min} = 2 \times 10^{-3}\ Pa$ and $p_{max} = 3 \times 10^{-3}$, respectively. Note that the maximum value belongs to the inlet, while the minimum value belongs to the outlet.

b. Comparison Between the MATLAB and COMSOL Results

In order to put our theoretical model to test and see how it performed with respect to the COMSOL model, we will be comparing results presented in Sec.3.a-b, providing us with insight into a comparative investigation between these two models.

To facilitate this, the key results of each model, which included velocity profiles and pressure distributions, have been illustrated with respect to each other in Fig.6, where Fig.6.a gives us an understanding of the velocity profiles yielded by both models, while Fig.6.b allows us to compare the pressure distributions of the respective models.
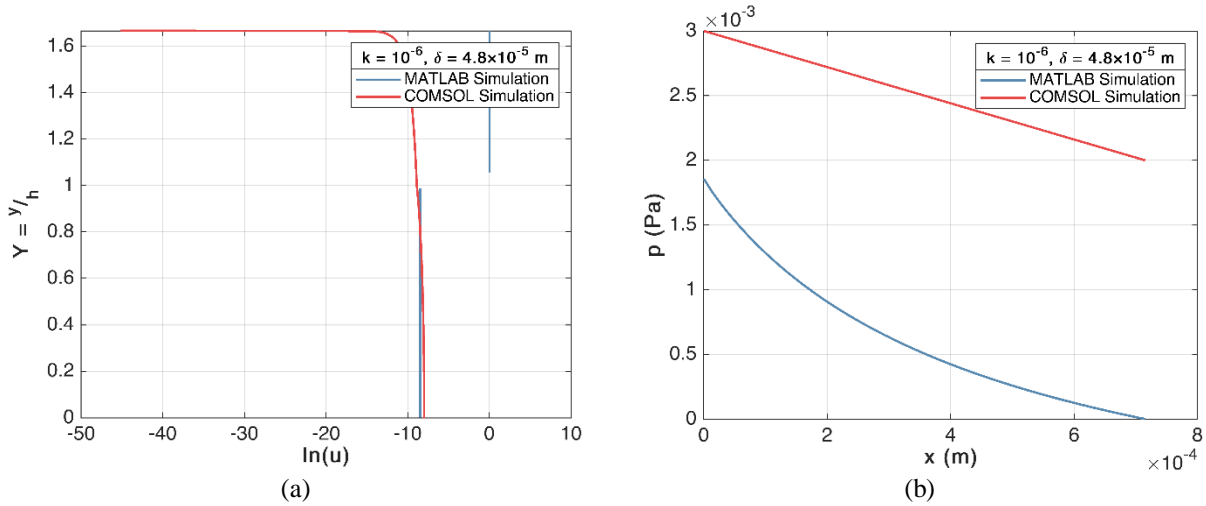
Figure 6: (a) shows Y versus the natural log of velocity, $\ln(u)$, for both models, while (b) shows the pressure along the microchannel yielded by the MATLAB and COMSOL model respectively.

As seen in Fig.6.a, the MATLAB and COMSOL model seem to be in apparent agreement with regard to the velocity order of magnitude in the core region. In the porous regions, however, our theoretical model, which is resembled by the blue line, model seems to vary considerably with respect to the velocity order of magnitude predicted by the Free and Porous Media Flow Module of the COMSOL model.

Similar disparities between the COMSOL and MATLAB model seem to exist in Fig.6.b, too. Yet, this difference seems to be negligibly small, as the variation is approximately $2 \times 10^{-3}\ Pa$ at most. Contrary to this difference, both models seem to predict roughly the same trend in regards to the variation of pressure with respect to x along the microchannel. The MATLAB model, however, does not predict a completely linear relationship and instead, suggests a trend similar to a convex function.

It is hypothesized that different governing equations and thus, different dependence on various parameters in addition to numerical errors in the MATLAB model gives rise to these differences. As an example, the COMSOL model did not take the inverse Knudsen number as an input parameter directly, even though our theoretical model was sensitive to variation of the inverse Knudsen number, signifying differences between the governing equations of the models presented in this paper. This difference, in particular, is demonstrated by how the COMSOL model makes use of the constitutive relation, including the Navier-Stokes equation, while the our model employs both Navier-Stokes and Darcy-Brinkman equations.

4. Conclusion

Boundary roughness plays a significant role on the flow inside microchannels. This effect gets particularly predominant when the free molecular path of the flow gets comparable to the characteristic length of a microchannel [4]. Due to its significance, it is mandatory that the roughness of the microchannel is taken into account in both modeling and manufacturing such channels, which have acquired considerable attraction due to their wide variety of their applications.

This crucial effect can be modelled using the simplified forms of Navier-Stokes and Darcy-Brinkman equations to derive analytical solutions for velocity and pressure, which probe information about the fluid flow inside the microchannel. In our paper, we have made us of this approach and derived velocity and pressure in the microchannel in addition to the mass flowrate inside the microchannel. To allow for further investigation of these parameters as functions of the inverse Knudsen number, porous media thickness and permeability, numerical results per different combinations of these variables were presented. After this, these numerical results were compared to the results yielded by another simulation, which was dependent on different governing equations. This comparison allowed for realizing both the similarities and differences between these models, one of which reflected our theoretical model, while the other represented a different theoretical model [Ref.a].

Even though the main goal of this work, which was to develop a theoretical model to take surface roughness into account, was achieved, we believe the future direction of this work would be to resolve the differences between our model and the model presented in Ref.a, allowing us to develop a rather comprehensive theoretical model. Furthermore, validating the velocity gap in core and porous regions, which were sudden changes in velocity values at

the borderlines of the free and porous areas, can provide researchers and manufacturers with valuable information with regard to whether this gap occurs in reality and whether it can be minimized.

Appendix A: A Closer Look at Velocity in Porous Regions

As explained in Sec.3.a, due to the large difference between velocity in core and porous regions, it would have been helpful to visualize the velocity in porous regions, too. This has been done in Fig.A-1. Please note that the velocity in the graphs, u, corresponds to $\tilde{u}$, which is velocity in the porous region.

(a)

(b)

(c)

(d)

(e)
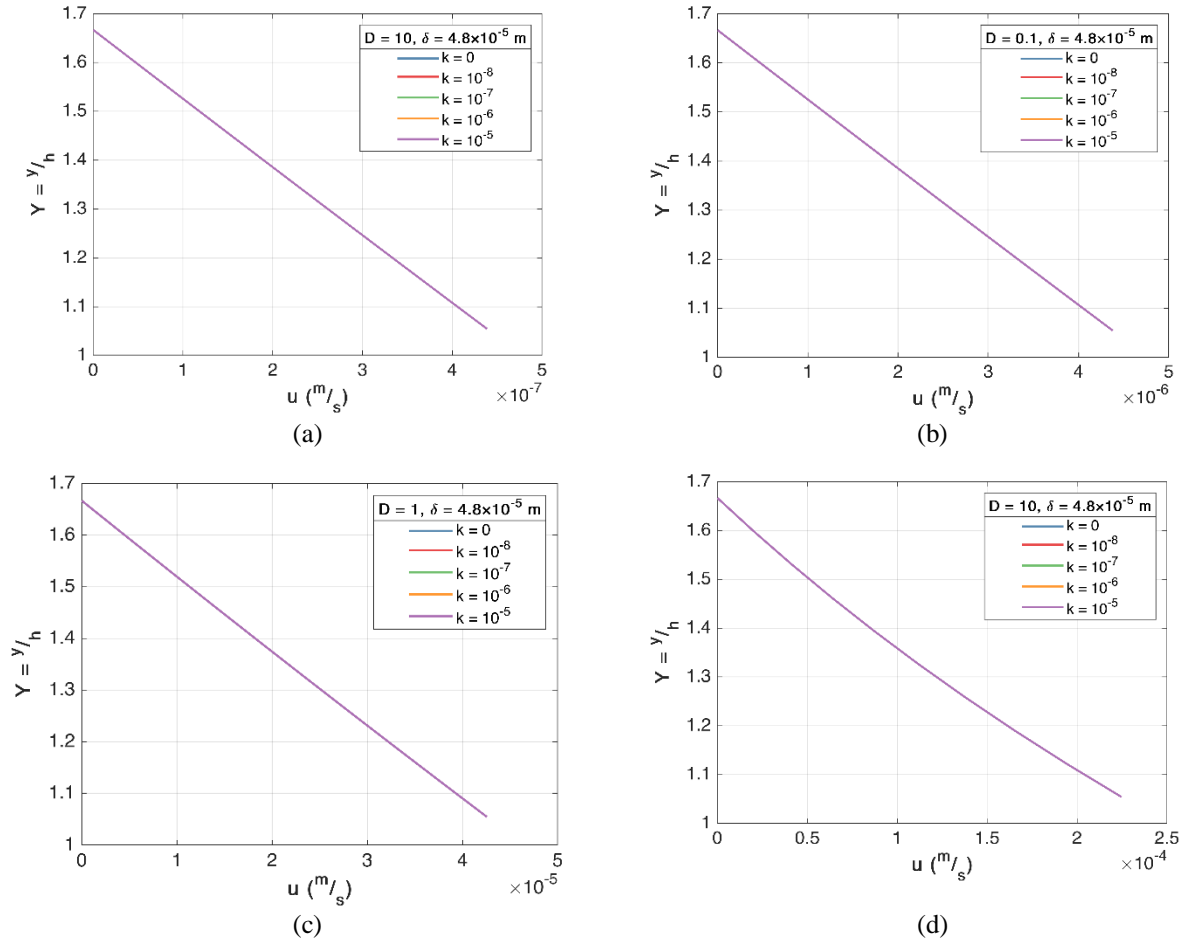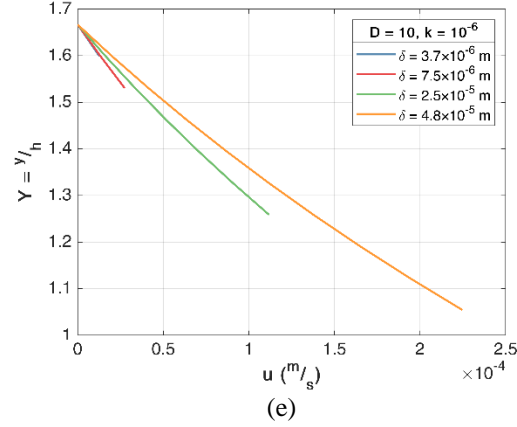
Figure A-1: This figure shows $\tilde{u}$, the velocity profile inside the porous regions per different values of the inverse Knudson number, permeability, and porous media thickness. The cases per different parameters are the same as the ones presented in Fig.2.

As seen in Fig.A-1, there seems to an approximately linear relationship between $\tilde{u}$ and Y. This trend, however, seems to become convex as the inverse Knudsen number increases, which is particularly demonstrated in Fig.A-1.d. Moreover, the order of magnitude of $\tilde{u}$ seems to increase at higher inverse Knudsen numbers. Different velocity orders of magntidue along with their inverse Knudsen numbers have been summarized in Table.A-1.

Figure	Inverse Knudsen Number and Regime	$\tilde{u}$ order of magnitude (m/s)
A-1.a	$D = 0.01$, Continuum-Slip Flow	10^{-7}
A-1.b	$D = 0.1$, Slip-Early Transition Flow	10^{-6}
A-1.c	$D = 1$, Early Transition-Transition Flow	10^{-5}
A-1.d	$D = 10$, Transition-Free Molecular Flow	10^{-4}

Table A-1: This table shows the change in velocity at different Knudsen numbers based on Figs.A-1.a-d.

Contrary to these changes, velocity inside the porous media seems to have negligible to no sensitivity to variations in permeability, which is demonstrated by how all lines are masked by the purple line. This, in addition to the points mentioned in the conclusion, seem to be good starting points for further investigations with regards to this work.

In Fig.A-1.e, different values of $\tilde{u}$ per various porous media thicknesses have been illustrated. Empty regions in the lines signify insolvability of $\tilde{u}$ at these values of Y. In this figure, variation with respect to porous media thickness can be seen, where velocity seems to change rather steeply at larger porous media thickness values. Moreover, as the porous media thickness increases, the velocity profile behaves rather similarly to a convex function, particularly in the case where $\delta = 4.8 \times 10^{-5} \, m$.

In addition to the lack of sensitivity to different values of k in Figs.A-1.a-d, another interesting direction of future works can be investigating the lack of yielding numerical results for $\tilde{u}$ per different values of δ, which is visible in Fig.A-1.e.

Appendix B: Pressure Per Different Values of Permeability and Porous Media Thickness

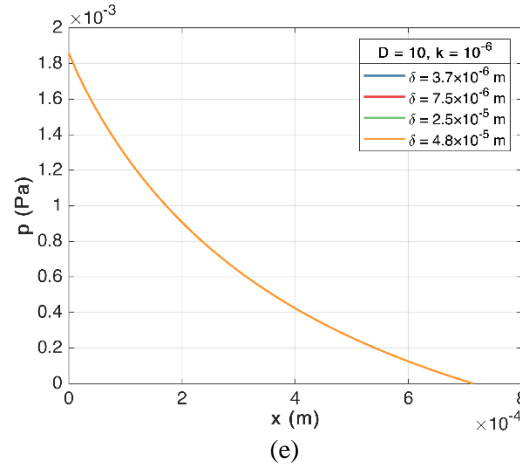Similar to Fig.2, Fig.B-1 includes a visualization of different combinations of permeability, k, and porous media thickness, δ.

(a)

(b)

(c)

(d)

(e)
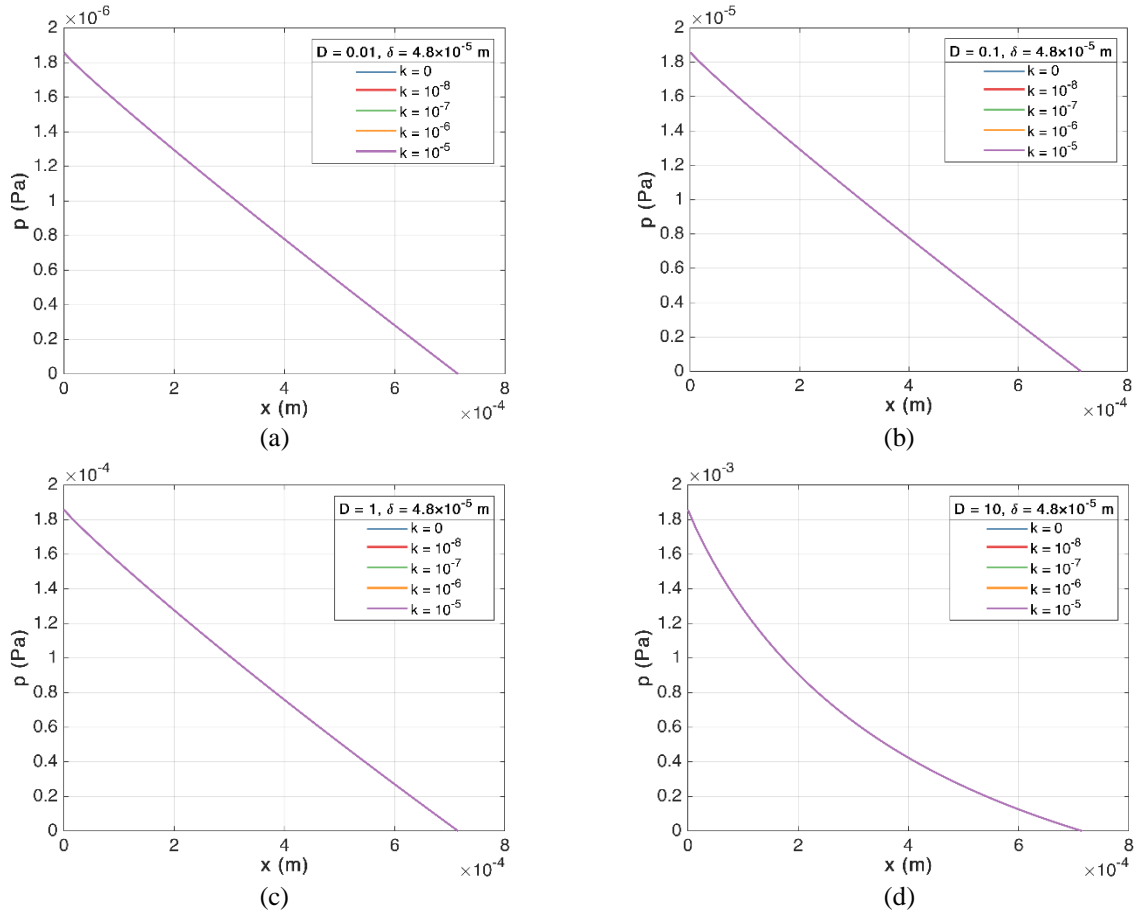
Figure B-1: This figure represents pressure at different values of the inverse Knudsen number and permeability (a-d), while also showing pressure per different values of porous media thickness (d).

The reason behind illustrating Fig.B-1 was to show the lack of sensitivity in pressure per different values of k and δ, even though pressure along the microchannel varies with respect to different values of D, which is the inverse Knudsen number. Validation of this remarkable behavior experimentally and further investigation of this characteristic theoretically will also be an interesting extension of this work in addition to the points mentioned in Sec.4 and App.A.

References

[1] Geete, A., & Pathak, R (2019) Effect of surface roughness on the performance of heat exchanger. SN Applied Sciences, 1(8), 901. https://doi.org/10.1007/s42452-019-0954-x

[2] Ardıçlıoğlu, M., & Kuriqi, A (2019) Calibration of channel roughness in intermittent rivers using HEC-RAS model: Case of Sarimsakli creek, Turkey. SN AppliedSciences, 1(9), 1080. https://doi.org/10.1007/s42452-019-1141-9

[3] Shiriny, A., Bayareh, M., Ahmadi Nadooshan, A. et al. (2019) Forced convection heat transfer of water/FMWCNT nanofluid in a microchannel with triangular ribs. SN Appl. Sci. 1, 1631. https://doi.org/10.1007/s42452-019-1678-7

[4] Fakher, S., Imqam (2012) A. Flow of carbon dioxide in micro and nano pores and its interaction with crude oil to induce asphaltene instability. SN Appl. Sci. 2, 1039. https://doi.org/10.1007/s42452-020-2850-9

[5] Ohadi, M., Choo, K., Dessiatoun, S., & Cetegen, E. (2013) Emerging applications of microchannels. In Next Generation Microchannel Heat Exchangers (pp. 67-105). Springer, New York, NY. https://doi.org/10.1007/978-1-4614-0779-9_3

[6] Bannari, R., Hilali, Y., Essadki, A. et al. (2019) Computational fluid dynamic for improving design and performance of an external loop airlift reactor used in electrochemical wastewater treatment. SN Appl. Sci. 1, 1497. https://doi.org/10.1007/s42452-019-1523-z

[7] Ong, Y.S., Ku Shaari, K (2020) CFD investigation of the effect of manifold and microchannel ratio on the hydrodynamic performance of microchannel heat sink. SN Appl. Sci. 2, 1199. https://doi.org/10.1007/s42452-020-2990-y

[8] Santana, H.S., Silva, J.L., Aghel, B. et al. (2020) Review on microfluidic device applications for fluids separation and water treatment processes. SN Appl. Sci. 2, 395. https://doi.org/10.1007/s42452-020-2176-7

[9] Garg, R., Agrawal, A (2019) Influence of three-dimensional transverse micro-ridges on the Poiseuille number in a gaseous slip flow. SN Appl. Sci. 1, 1035. https://doi.org/10.1007/s42452-019-0991-5

[10] Gamrat, G., Favre-Marinet, M., Le Person, S., Baviere, R., & Ayela, F (2008) An experimental study and modelling of roughness effects on laminar flow in microchannels. Journal of Fluid Mechanics, 594, 399. https://doi.org/10.1017/S0022112007009111

[11] Tang, G. H., Li, Z., He, Y. L., & Tao, W. Q (2007) Experimental study of compressibility, roughness and rarefaction influences on microchannel flow. International Journal of Heat and Mass Transfer, 50(11-12), 2282-2295. https://doi.org/10.1016/j.ijheatmasstransfer.2006.10.034

[12] Jones, B. J., and Garimella, S. V (2010) "Surface Roughness Effects on Flow Boiling in Microchannels." ASME. J. Thermal Sci. Eng. Appl. 1(4): 041007. https://doi.org/10.1115/1.4001804

[13] Wu, H. Y., & Cheng, P (2003) An experimental study of convective heat transfer in silicon microchannels with different surface conditions. International journal of heat and mass transfer, 46(14), 2547-2556. https://doi.org/10.1016/S0017-9310(03)00035-8

[22] Khadem, M. H., Shams, M., & Hossainpour, S (2009) Numerical simulation of roughness effects on flow and heat transfer in microchannels at slip flow regime. International Communications in Heat and Mass Transfer, 36(1), 69-77. https://doi.org/10.1016/j.icheatmasstransfer.2008.10.009

[23] Sun, H., & Faghri, M (2003) Effect of surface roughness on nitrogen flow in a microchannel using the direct simulation Monte Carlo method. Numerical Heat Transfer: Part A: Applications, 43(1), 1-8. https://doi.org/10.1080/10407780307302

[24] Wang, M., Wang, J., & Chen, S (2007) Roughness and cavitations effects on electro-osmotic flows in rough microchannels using the lattice Poisson–Boltzmann methods. Journal of Computational Physics, 226(1), 836-851. https://doi.org/10.1016/j.jcp.2007.05.001

[25] Yang, D., & Liu, Y (2008) Numerical simulation of electroosmotic flow in microchannels with sinusoidal roughness. Colloids and Surfaces A: Physicochemical and Engineering Aspects, 328(1-3), 28-33. https://doi.org/10.1016/j.colsurfa.2008.06.029

[26] W. Li, J. Lin, S. Lee, M. Chen (2002) Effects of Roughness on Rarefied Gas Flow in Long Microtubes , Journal of Micromechanics and Microengineering. 12, 149-156.https://doi.org/10.1088/0960-1317/12/2/308

[27] Meyerovich, A. E., & Stepaniants, S (1994) Transport phenomena at rough boundaries. Physical review letters, 73(2), 316. https://doi.org/10.1103/PhysRevLett.73.316

[28] Meyerovich, A. E., & Stepaniants, S (1997) Ballistic transport in ultra-thin films with random rough walls. Journal of Physics: Condensed Matter, 9(20), 4157. https://doi.org/10.1088/0953-8984/9/20/015

[29] Karniadakis, G., Beskok, A., & Aluru, N. (2006) Microflows and nanoflows: fundamentals and simulation (Vol. 29). Springer Science & Business Media.

[30] Powell, C. E., & Silvester, D. J (2012) Preconditioning steady-state Navier--Stokes equations with random data. SIAM Journal on Scientific Computing, 34(5), A2482-A2506. https://doi.org/10.1137/120870578

[31] Liu, H., Patil, P. R., & Narusawa, U (2007) On Darcy-Brinkman equation: viscous flow between two parallel plates packed with regular square arrays of cylinders. Entropy, 9(3), 118-131. https://doi.org/10.3390/e9030118

[32] Norouzi, A. M., Siavashi, M., Soheili, A. R., & Oskouei, M. K (2018) Experimental investigation of effects of grain size, inlet pressure and flow rate of air and argon on pressure drop through a packed bed of granular activated carbon. International Communications in Heat and Mass Transfer, 96, 20-26. https://doi.org/10.1016/j.icheatmasstransfer.2018.05.019

[33] Titelman, L (2019) Generalized variables for both porous and ordered mesoporous materials. SN Applied Sciences,1(10), 1294. https://doi.org/10.1007/s42452-019-1318-2

[34] Li, W. L., & Hwang, C. C (1999) Derivation of the modified molecular gas lubrication equation-a porous media model. Journal of Physics D: Applied Physics, 32(12), 1421. https://doi.org/10.1088/0022-3727/32/12/320

[a] https://doc.comsol.com/5.5/doc/com.comsol.help.porous/IntroductionToPorousMediaFlowModule.pdf